PHYSICS

The spin Nernst effect in tungsten

Peng Sheng,[1] Yuya Sakuraba,[1] Yong-Chang Lau,[1,2] Saburo Takahashi,[3] Seiji Mitani,[1,4] Masamitsu Hayashi[1,2]*

Copyright © 2017 The Authors, some rights reserved; exclusive licensee American Association for the Advancement of Science. No claim to original U.S. Government Works. Distributed under a Creative Commons Attribution NonCommercial License 4.0 (CC BY-NC).

The spin Hall effect allows the generation of spin current when charge current is passed along materials with large spin-orbit coupling. It has been recently predicted that heat current in a nonmagnetic metal can be converted into spin current via a process referred to as the spin Nernst effect. We report the observation of the spin Nernst effect in W. In W/CoFeB/MgO heterostructures, we find changes in the longitudinal and transverse voltages with magnetic field when temperature gradient is applied across the film. The field dependence of the voltage resembles that of the spin Hall magnetoresistance. A comparison of the temperature gradient–induced voltage and the spin Hall magnetoresistance allows direct estimation of the spin Nernst angle. We find the spin Nernst angle of W to be similar in magnitude but opposite in sign to its spin Hall angle. Under an open-circuit condition, this sign difference results in the spin current generation larger than otherwise. These results highlight the distinct characteristics of the spin Nernst and spin Hall effects, providing pathways to explore materials with unique band structures that may generate large spin current with high efficiency.

INTRODUCTION

The giant spin Hall effect (SHE) (*1*) in heavy metals (HMs) with large spin-orbit coupling has attracted great interest owing to its potential use as a spin current source to manipulate magnetization of magnetic layers (*2*–*4*). Recently, it has been reported (*5*, *6*) that the spin Hall conductivity of 5*d* transition metals depends on the number of 5*d* electrons, indicating that the observed SHE is due to the topology and filling of the characteristic bands at the Fermi surface (*7*, *8*). Spin current in solids can be produced not only by charge current but also by heat current (*9*). Understanding the coupling between spin current and heat current is the central subject of spin caloritronics (*10*). It is now well understood that a temperature gradient applied across a magnetic material, typically a magnetic insulator, results in spin accumulation that can be used to generate spin current in neighboring nonmagnetic materials via the spin Seebeck effect (*11*–*17*).

It has been predicted theoretically (*18*–*23*) that in nonmagnetic materials with strong spin-orbit coupling, the heat current can be converted into spin current. The effect, often referred to as the spin Nernst effect, generates spin current that scales with the energy derivative of the spin Hall conductivity. Here, we show direct probe of the spin Nernst effect in amorphous-like W, which has the largest spin Hall angle among the 5*d* transition metals (*6*, *24*, *25*). When an in-plane temperature gradient is applied across W/CoFeB/MgO heterostructures, we observe longitudinal and transverse voltages that vary with the magnetic field similar to those of the spin Hall magnetoresistance (SMR) (*26*–*31*). The W layer thickness dependence of the longitudinal voltage is compared to that of the SMR to estimate the size and sign of the spin Nernst angle. We find that the spin Nernst angle of W is slightly smaller (~70%) than its spin Hall angle and the two angles have opposite signs.

RESULTS

The film structure used is sub.|d_N HM|1 FM|2 MgO|1 Ta (thickness in nanometers), where HM is Ta or W and the ferromagnetic metal (FM) is $Co_{20}Fe_{60}B_{20}$ (hereafter referred to as CoFeB). We first study the electrical transport properties of the films. The inverse of the device longitudinal resistance ($1/R_{XX}$) multiplied by a geometrical factor (L/w), the sheet conductance $G_{XX} = L/(wR_{XX})$, is plotted as a function of the HM layer thickness (d_N) in Fig. 1 (A and B) for the Ta and W underlayer films, respectively (see inset of Fig. 1A for the definitions of L and w as well as the coordinate system). We fit the data with a linear function to estimate the resistivity (ρ_N) of the HM layer. The fitting results are shown by the blue solid lines: We obtain ρ_N of ~183 and ~130 μΩ·cm for Ta and W, respectively. Note that W undergoes a structural phase transition (*6*, *24*, *32*) when its thickness is larger than ~6 nm, as indicated by the change in G_{XX} at this thickness. The SMR, $R_{SMR} = \Delta R_{XX}/R_{XX}^{Z}$, is plotted as a function of the HM layer thickness in Fig. 1 (C and D). We define $\Delta R_{XX} = R_{XX}^{Y} - R_{XX}^{Z}$ as the resistance difference when the magnetization of the CoFeB layer is pointing along the y direction (R_{XX}^{Y}) and z direction (R_{XX}^{Z}). The thickness dependence of R_{SMR} is consistent with previous reports (*6*, *31*).

The transverse resistance of the films is shown in Fig. 2 (see inset of Fig. 1A for details of the measurement setup). The inset of Fig. 2A shows the transverse resistance (R_{XY}) versus the out-of-plane field H_Z for a Ta underlayer film. We define $2\Delta R_{XY} = R_{XY}^{Z} - R_{XY}^{-Z}$, that is, the anomalous Hall resistance, as the difference in R_{XY} when the magnetization is pointing along $+z$ and $-z$. In Fig. 2 (A and B), ΔR_{XY} is plotted as a function of HM layer thickness. $|\Delta R_{XY}|$ decreases with increasing d_N largely due to current shunting into the HM layer. To estimate the anomalous Hall angle, ΔR_{XY} is divided by R_{XX}^{Z}, multiplied by a geometric factor (L/w), and divided by a constant (x_F) that accounts for the current shunting effect into the HM layer: $x_F = \frac{t_F\rho_N}{t_F\rho_N + d_N\rho_F}$, where t_F and ρ_F are the thickness and resistivity of the FM layer, respectively. The HM layer thickness dependence of the normalized anomalous Hall coefficient $R_{AHE}/x_F = (\Delta R_{XY}L)/(R_{XX}^{Z}wx_F)$ is plotted in Fig. 2 (C and D) for the Ta and W underlayer films, respectively. We find that the normalized anomalous Hall coefficient shows a significant HM layer thickness dependence, particularly for the W underlayer films.

We next show the thermoelectric properties of the films. Figure 3A shows a sketch of the setup to study the Seebeck coefficient of the films. A heater is placed near one side of the substrate to create a temperature gradient across the substrate. The difference in the temperature between the hot (T_H) and cold (T_L) sides of the substrate ($\Delta T = T_H - T_L$), across a distance D, is measured using an infrared camera. The longitudinal

[1]National Institute for Materials Science, Tsukuba 305-0047, Japan. [2]Department of Physics, The University of Tokyo, Bunkyo, Tokyo 113-0033, Japan. [3]Institute for Materials Research, Tohoku University, Sendai 980-8577, Japan. [4]Graduate School of Pure and Applied Sciences, University of Tsukuba, Tsukuba 305-8577, Japan. *Corresponding author. Email: hayashi@phys.s.u-tokyo.ac.jp

Downloaded from http://advances.sciencemag.org/ on January 24, 2021

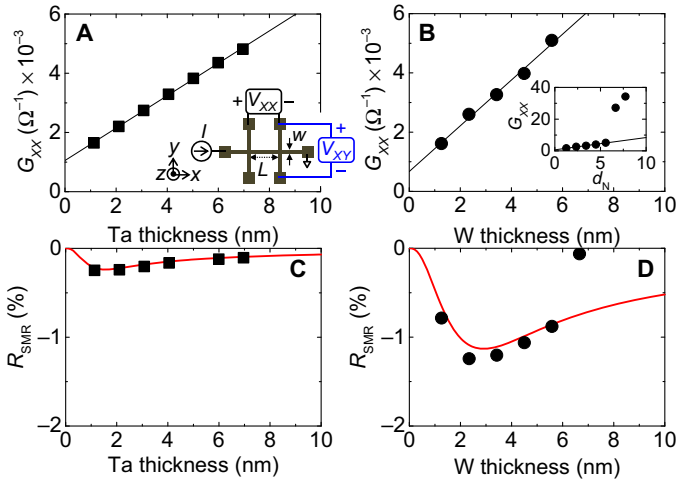

Fig. 1. Longitudinal resistance and SMR of HM|CoFeB|MgO heterostructures. (**A** and **B**) Sheet conductance $G_{XX} = L/(wR_{XX})$ versus HM layer thickness d_N for the Ta (A) and W (B) underlayer films. The solid lines show a linear fit to the data in an appropriate range of d_N. Schematic of the measurement setup is illustrated in the inset of (A). The inset of (B) is the expanded *y*-axis plot of the main panel. (**C** and **D**) SMR ($R_{SMR} = \Delta R_{XX}/R_{XX}^{Z}$) plotted against d_N for the Ta (C) and W (D) underlayer films. The red solid lines are fit to the data using Eq. 1. Parameters used in the fitting are summarized in Table 1.

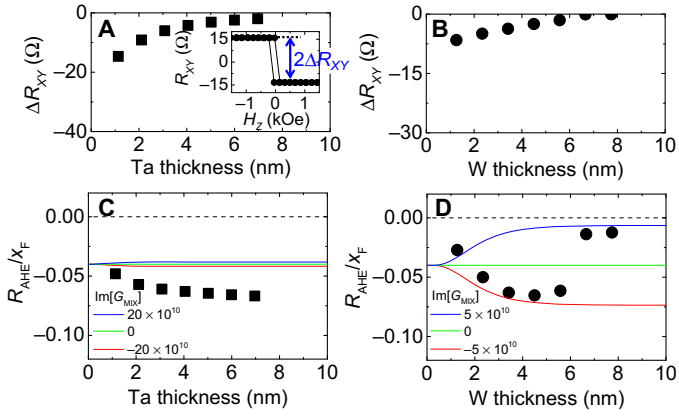

Fig. 2. HM layer thickness dependence of the anomalous Hall resistance. (**A** and **B**) HM layer thickness (d_N) dependence of the anomalous Hall resistance (ΔR_{XY}) for the Ta (A) and W (B) underlayer films. The inset of (A) shows R_{XY} versus H_Z for sub.|~1.1 Ta|1 CoFeB|2 MgO|1 Ta (thickness in nanometers). The definition of ΔR_{XY} is schematically illustrated. (**C** and **D**) Normalized anomalous Hall coefficient $R_{AHE}/x_F = (\Delta R_{XY}L)/(wR_{XX}^{Z}x_F)$ plotted against d_N for the Ta (C) and W (D) underlayer films. The solid lines show the calculated R_{AHE}/x_F using Eq. 2 with three different values of Im[G_{MIX}]. Parameters used in the calculations are summarized in Table 1, except for Im[G_{MIX}], which is noted in the legend.

(Seebeck) voltage $V_{XX} = V(x_1) - V(x_2)$ is measured between two points of the device separated by a distance $L = x_2 - x_1 < D$. The temperature of position x_1 is higher than that of x_2 (see Fig. 3A). The ΔT dependence of V_{XX} is shown in Fig. 3 (B and C) for the Ta and W underlayer films, respectively. The data are fitted with a linear function to extract the Seebeck coefficient $S \sim -(V_{XX}/L)/(\Delta T/D)$ (*33*) from the slope, which is plotted as a function of d_N in Fig. 3 (D and E). S approaches ~−4 μV/K when the HM layer thickness is thin for both film structures, which we consider provides information of the Seebeck coefficient of CoFeB (we assume that the MgO and the oxidized Ta capping layers have negligible contribution to V_{XX}). In contrast, the thick limit of d_N gives the Seebeck coefficient of the HM layer: We estimate S of ~−2 and ~−12 μV/K for Ta and W, respectively.

The off-diagonal component of the thermoelectric properties is summarized in Fig. 4. The experimental setup to study the temperature gradient–induced transverse voltage is depicted in Fig. 4A. A typical hysteresis loop obtained by measuring the H_Z dependence of the temperature gradient–induced transverse voltage $V_{XY} = V_{XY}(y_2) - V_{XY}(y_1)$ (see Fig. 4A for the definitions of y_1 and y_2) is shown in Fig. 4B. Similar to the anomalous Hall resistance, we define $2\Delta V_{XY}$, that is, the anomalous Nernst voltage, as the difference in V_{XY} when the magnetization is pointing along +*z* and −*z*. Figure 4C shows the ΔT dependence of ΔV_{XY} for a W underlayer film. Within the applied temperature gradient, the response is linear. We thus fit a linear function to obtain the anomalous Nernst coefficient $S_{ANE} = (\Delta V_{XY}/L)/(\Delta T/D)$ from the slope (here, $L = y_2 - y_1$).

The HM layer thickness dependence of anomalous Nernst coefficient S_{ANE} is plotted for the Ta and W underlayer films in Fig. 4 (D and E, respectively). $|S_{ANE}|$ decreases with increasing d_N for the Ta underlayer films, whereas it shows a peak at around $d_N \sim 3$ nm for the W underlayer films. Similar to the anomalous Hall resistance, the presence of the HM layer can shunt the Hall voltage. To account for this effect, S_{ANE} is divided by x_F. The normalized anomalous Nernst coefficient S_{ANE}/x_F is plotted as a function of d_N in Fig. 4 (F and G). We find a larger variation of S_{ANE}/x_F with d_N for the W underlayer films than that for the Ta underlayer films.

Recent studies have shown that the spin current generated within the HM layer modifies the anomalous Hall resistance via a nonzero imaginary part of the spin-mixing conductance at the HM/FM interface (*26*, *27*, *34*). The large variation of the normalized anomalous Nernst coefficient with d_N for the W underlayer films indicates that a temperature gradient can cause the spin current generation in the W layer that results in the modification of the off-diagonal component. To evaluate the temperature gradient–induced spin current generation (due to the spin Nernst effect) in a more explicit way, we studied the external field dependence of the Seebeck voltage in analogy to the SMR. The experimental setup is the same with that of Fig. 3A: Here, a large external magnetic field is applied during the measurements.

In Fig. 5 (A and B), we show the longitudinal (Seebeck) voltage $V_{XX} = V(x_1) - V(x_2)$ of Ta and W underlayer films, respectively, plotted as a function of the external field directed along the *y* axis (H_Y). The temperature difference ΔT across the substrate is ~3.5 K. For the W underlayer films (Fig. 5B), we find a peak-like structure around zero field (signals are shifted vertically for clarity so that the large field limit of V_{XX} is equal to zero). The peak found in the V_{XX} versus H_Y plot decays to zero when $|H_Y| \sim |H_K|$, where H_K is the effective anisotropy field required to force the magnetization to point along the film plane (see fig. S1 for the magnetic properties of the heterostructures). The peak amplitude $\Delta V_{XX} = V_{XX}^{Y} - V_{XX}^{Z}$ defined schematically in Fig. 5B is equivalent to the difference in V_{XX} when the magnetization is pointing along the *y* axis (V_{XX}^{Y}) and the *z* axis (V_{XX}^{Z}). This definition is in accordance to that of SMR. We have also studied V_{XX} as a function of H_X and H_Z (the results are shown in fig. S2). In contrast to V_{XX} versus H_Y, we find no clear feature in the H_X and H_Z dependence of V_{XX}. These results suggest that the thermal analog of the anisotropic magnetoresistance (AMR) is small in CoFeB (*35*). Note that the AMR of the CoFeB layer here is ~0.1% (*31*), much smaller than that of the Ni-based soft magnetic materials (*36*). The small temperature gradient–induced AMR-like voltage (V_{XX} versus H_X; see fig. S2) found here also indicates

Downloaded from http://advances.sciencemag.org/ on January 24, 2021

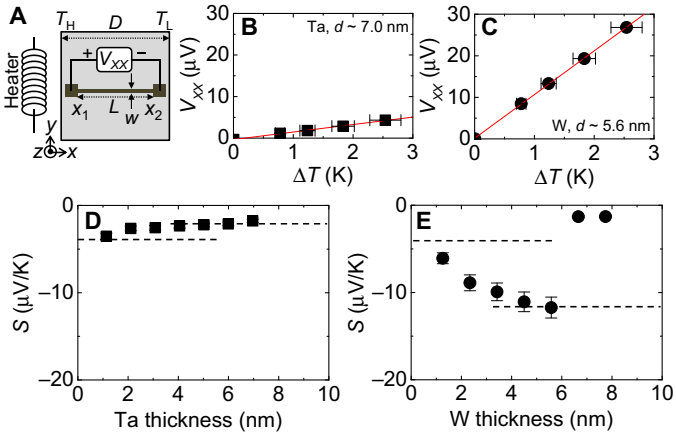

Fig. 3. Seebeck coefficient of HM|CoFeB|MgO heterostructures. (**A**) Schematic illustration of the measurement setup for temperature gradient–induced longitudinal voltage. The bright square represents part of the substrate, and the dark region indicates the area where the device is located. D = 0.7 cm; L = 0.6 cm; w = 50 μm. (**B** and **C**) Longitudinal (Seebeck) voltage V_{XX} measured as a function of the temperature difference ΔT for sub.|~7.0 Ta|1 CoFeB|2 MgO|1 Ta (B) and sub.|~5.6 W|1 CoFeB|2 MgO|1 Ta (C). The horizontal and vertical error bars represent the uncertainty of the temperature gradient and the variation of the voltage under a fixed temperature gradient, respectively. (**D** and **E**) Seebeck coefficient $S \sim -(V_{XX}/L)/(\Delta T/D)$ plotted against d_N for the Ta (D) and W (E) underlayer films. The error bars denote the variation of S due to the uncertainty of the temperature gradient. The horizontal dashed lines are guides to the eye, which provide an estimate of the Seebeck coefficient of the HM and FM layers.

that the possible contribution from the combination of AMR and interfacial spin-orbit coupling (*37*, *38*) on ΔV_{XX} may be small. We also find little evidence of proximity-induced magnetism (*39*–*41*) in W and Ta, which may influence the temperature gradient–induced voltage via AMR in the HM layer.

In Fig. 5C, we plot $S_{SNE} = (\Delta V_{XX}/L)/(\Delta T/D)$, which we refer to as the spin Nernst coefficient, as a function of the W layer thickness. $|S_{SNE}|$ takes a maximum at $d_N \sim 3$ to 4 nm, similar to that of the SMR shown in Fig. 1D. These results indicate that the interfacial magnetoresistance caused by the Rashba interaction, which takes a maximum at an HM layer thickness close to one lattice constant (*42*), is not the main source of the voltage (S_{SNE}) found here [see figs. S3 and S4 for discussions on the effects of the FM layer (CoFeB) and an unintended out-of-plane temperature gradient (*15*, *43*–*45*) on the voltage measurements].

To account for these results, a drift-diffusion model is extended to describe spin transport in a bilayer system. The HM layer thickness dependence of the SMR and the anomalous Hall coefficient are described by the following equations (*26*, *31*)

$$R_{SMR} \equiv \frac{\Delta R_{XX}}{R_{XX}^{Z}} = -(1-x_F)\theta_{SH}^2 \frac{\lambda_N}{d_N} \tanh^2\left(\frac{d_N}{2\lambda_N}\right) \mathrm{Re}\left[\frac{g_S}{1+g_S \coth(d_N/\lambda_N)}\right] \quad (1)$$

$$R_{AHE} \equiv \frac{\Delta R_{XY}}{R_{XX}^{Z}} \frac{L}{w} = -x_F\theta_{AH} + (1-x_F)\theta_{SH}^2 \frac{\lambda_N}{d_N} \tanh^2\left(\frac{d_N}{2\lambda_N}\right) \mathrm{Im}\left[\frac{g_S}{1+g_S \coth(d_N/\lambda_N)}\right] \quad (2)$$

where θ_{SH} and λ_N are the spin Hall angle and the spin diffusion length of the HM layer, respectively; θ_{AH} is the anomalous Hall angle of the FM layer; and $g_S = 2\rho_N\lambda_N G_{MIX}$, where G_{MIX} is the spin-mixing conductance of the HM/FM interface. Here, for simplicity, we have neglected the contribution of longitudinal spin current absorption on the SMR (*31*).

Furthermore, we assume that a temperature gradient (∇T) applied across a sample can generate spin current **Q** (flow of spin angular momentum carried by electrons) via the spin Nernst effect in a similar way an electric field **E** (or current) generates spin current through the SHE, that is

$$Q_{kj} = \frac{\hbar}{2|e|}\theta_{SH}\left(\mathbf{e}_k \times \frac{\mathbf{E}}{\rho_N}\right)\Big|_j + \frac{\hbar}{2|e|}\theta_{SN}\left(\mathbf{e}_k \times \frac{S_N}{\rho_N}(-\nabla T)\right)\Big|_j \quad (3)$$

where indices k and j denote the spin and flow direction of the spin current, respectively; $\mathbf{e}_k$ is a unit vector; $\hbar$ is the reduced Planck constant; e is the electron's charge; and S_N and θ_{SN} are the Seebeck coefficient and the spin Nernst angle of the HM layer, respectively. For simplicity, we do not consider the spin Hall and spin Nernst effects of the FM layer because θ_{SH} of FM has been reported to be small compared to that of the HM layers (*46*–*48*). However, in the FM layer, the anomalous Hall and anomalous Nernst effects generate a transverse charge current $\mathbf{J}^T$ when **E** and ∇T are applied. The transverse charge current (opposite to the electron flow) is

$$J_j^T = -\theta_{AH}\left(\mathbf{m} \times \frac{\mathbf{E}}{\rho_F}\right)\Big|_j - \theta_{AN}\left(\mathbf{m} \times \frac{S_F}{\rho_F}(-\nabla \boldsymbol{T})\right)\Big|_j \quad (4)$$

where **m** is a unit vector representing the magnetization direction of the FM layer, and S_F and θ_{AN} are the Seebeck coefficient and the anomalous Nernst angle of the FM layer, respectively.

We assume that a temperature gradient $\frac{\Delta T}{D} = \frac{T_H - T_L}{D}$ is applied under an open-circuit condition. The change in the longitudinal voltage $\left(\frac{V_{XX}}{L} = \frac{V_{XX}(x_1) - V_{XX}(x_2)}{x_2 - x_1}\right)$ when the magnetization of the FM layer is pointing along the y axis (V_{XX}^{Y}) and z axis (V_{XX}^{Z}), $\Delta V_{XX} = V_{XX}^{Y} - V_{XX}^{Z}$, is expressed as

$$S_{SNE} \equiv \frac{\Delta V_{XX}/L}{\Delta T/D} = (1-x_F)\theta_{SH}\{\theta_{SH}S - \theta_{SN}S_N\}\frac{\lambda_N}{d_N}\tanh^2\left(\frac{d_N}{2\lambda_N}\right) \times \mathrm{Re}\left[\frac{g_S}{1+g_S \coth(d_N/\lambda_N)}\right] \quad (5)$$

Similarly, the difference in the transverse voltage $\left(\frac{V_{XY}}{L} = \frac{V_{XY}(y_2) - V_{XY}(y_1)}{y_2 - y_1}\right)$ when the magnetization reverses its direction from $+z$ to $-z$, $2\Delta V_{XY} = V_{XY}^{Z} - V_{XY}^{-Z}$, reads

$$S_{ANE} \equiv \frac{\Delta V_{XY}/L}{\Delta T/D} = x_F\{\theta_{AH}S - \theta_{AN}S_F\} - (1-x_F)\theta_{SH}\{\theta_{SH}S - \theta_{SN}S_N\}\frac{\lambda_N}{d_N} \times \tanh^2\left(\frac{d_N}{2\lambda_N}\right)\mathrm{Im}\left[\frac{g_S}{1+g_S \coth(d_N/\lambda_N)}\right] \quad (6)$$

Downloaded from http://advances.sciencemag.org/ on January 24, 2021

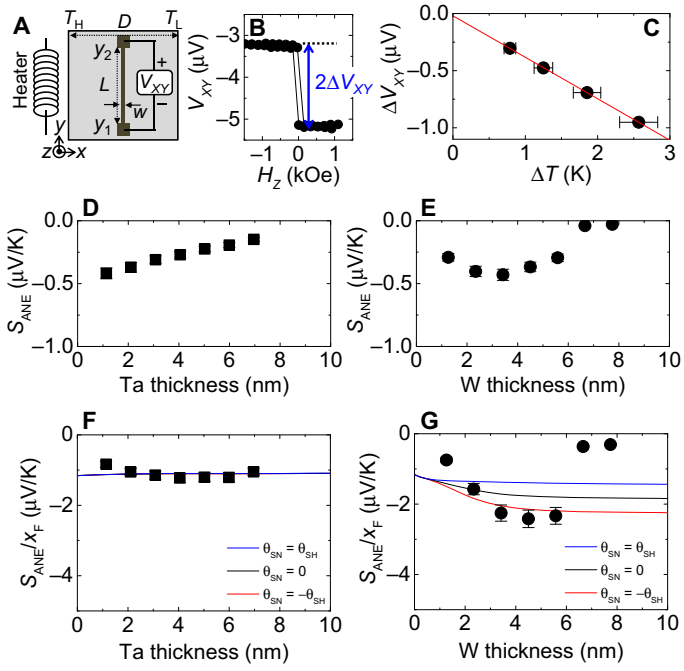

Fig. 4. HM layer thickness dependence of the anomalous Nernst effect. (**A**) Schematic illustration of the measurement setup for temperature gradient–induced transverse voltage. The bright square represents part of the substrate, and the dark region indicates the area where the device is located. D = 0.7 cm; L = 0.6 cm; w = 50 μm. (**B**) Transverse voltage V_{XY} versus H_Z of sub.|~3.4 W|1 CoFeB|2 MgO|1 Ta when a temperature difference of ΔT ~ 2.5 K is applied. The definition of ΔV_{XY} is schematically drawn by the blue arrow. (**C**) ΔT dependence of the anomalous Nernst voltage ΔV_{XY} for the same sample described in (B). The horizontal and vertical error bars represent the uncertainty of the temperature gradient and the variation of the voltage under a fixed temperature gradient, respectively. The red solid line shows a linear fit to the data. (**D** and **E**) Anomalous Nernst coefficient $S_{ANE} = (\Delta V_{XY}/L)/(\Delta T/D)$ plotted against d_N for the Ta (D) and W (E) underlayer films. (**F** and **G**) d_N dependence of the normalized anomalous Nernst coefficient $S_{ANE}/x_F = (\Delta V_{XY}D)/(L\Delta T x_F)$ for the Ta (F) and W (G) underlayer films. The error bars in (D) to (G) denote the variation of quantities due to the uncertainty of the temperature gradient. The solid lines in (F) and (G) show the calculated S_{ANE}/x_F using Eq. 6 with three different values of θ_{SN}. Parameters used in the calculations are summarized in Table 1.

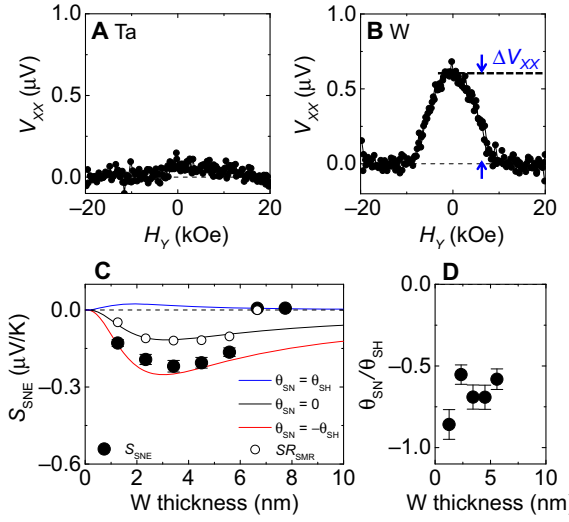

Fig. 5. Signatures of the spin Nernst magnetoresistance. (**A** and **B**) Longitudinal (Seebeck) voltage V_{XX} versus H_Y for sub.|~3.1 Ta|1 CoFeB|2 MgO|1 Ta (A) and sub.|~3.4 W|1 CoFeB|2 MgO|1 Ta (B) when a temperature difference ΔT of ~3.5 K is applied. The definition of ΔV_{XX} is schematically drawn. (**C**) d_N dependence of spin Nernst coefficient $S_{SNE} = (\Delta V_{XX}/L)/(\Delta T/D)$ (solid circles) and the scaled SMR SR_{SMR} (open circles) for the W underlayer films. The solid lines show the calculated S_{SNE} using Eq. 5 with three different values of θ_{SN}. Parameters used in the calculations are summarized in Table 1. (**D**) d_N dependence of θ_{SN}/θ_{SH} obtained from $S_{SNE}/(SR_{SMR})$ and the relation described in Eq. 7. The error bars in (C) and (D) denote the variation of quantities due to the uncertainty of the temperature gradient.

Equations 5 and 6 represent the d_N dependence of the spin Nernst and anomalous Nernst coefficients, respectively. The Seebeck coefficient of the HM/FM bilayer, defined as $S = x_F S_F + (1 - x_F)S_N$, is obtained experimentally using the relation $S \sim -(V_{XX}/L)/(\Delta T/D)$, and the results are shown in Fig. 3 (D and E). We note that when $\theta_{SN} = 0$, $S_{SNE} = SR_{SMR}$: The functional form of S_{SNE} and R_{SMR} is the same.

The first term ($\theta_{SH}S$) in the curly bracket of Eq. 5 appears because of the open-circuit condition. The electrons initially move from the hot to cold side when a temperature gradient is applied (the Seebeck coefficients of the FM and HM layers are all negative). Once the electrons reach the edge of the patterned structure, an internal electric field $\mathbf{E}_{INT}$ develops because of charge accumulation at the edges. The direction of $\mathbf{E}_{INT}$ is such that it cancels the electron flow driven by the temperature gradient, resulting in a net zero current. However, spin current can be generated via the SHE when a nonzero $\mathbf{E}_{INT}$ exists, thus contributing to the SMR. The second term ($\theta_{SN}S_N$) in the curly bracket of Eq. 5 corresponds to the contribution to the SMR that results from a direct conversion of heat current to spin current. Similar classification also applies to the terms in the curly brackets of Eq. 6.

The model calculations are compared to the experimental results presented in Figs. 1 (C and D), 2 (C and D), 4 (F and G), and 5C to find a parameter set that best describes the results. The calculation results are shown by the solid lines in each figure, and the parameters extracted (θ_{SH}, θ_{AH}, λ_N, θ_{SN}, θ_{AN}, Re[G_{MIX}], and Im[G_{MIX}]) are summarized in Table 1 (see Materials and Methods for details of the fitting process). The spin Hall angles (θ_{SH}) estimated for the Ta and W underlayers are consistent with those from previous reports (*2*, *6*, *24*, *25*, *31*). These results show that the model can account for all results shown in Figs. 1 to 5 using a single set of parameters listed in Table 1. Note that the spin-mixing conductance obtained from the fitting is mostly consistent with that from previous reports (see Materials and Methods for details).

To illustrate the effect of the spin Nernst effect on the transport properties more clearly, the spin Nernst and anomalous Nernst coefficients are numerically calculated using Eqs. 5 and 6 with three different spin Nernst angles, $\theta_{SN} = -\theta_{SH}$, $\theta_{SN} = 0$, and $\theta_{SN} = \theta_{SH}$. The open circles in Fig. 5C represent the scaled SMR (SR_{SMR}) calculated using the results of Figs. 1D and 3E. As described above, SR_{SMR} lies on the $\theta_{SN} = 0$ line. This demonstrates that the internal electric field $\mathbf{E}_{INT}$ partly contributes to the spin current generation. In contrast, the spin Nernst coefficient S_{SNE} (solid circles) lies closer to the $\theta_{SN} = -\theta_{SH}$ line. When the signs of θ_{SN} and θ_{SH} are opposite, contribution from the heat current–induced spin current adds constructively to the $\mathbf{E}_{INT}$-induced spin current. Note that for the Ta underlayer films, the expected spin Nernst coefficient using Eq. 5 and the parameters defined in Table 1 (with $\theta_{SN} = -\theta_{SH}$) is ~0.01 (μV/K). This is smaller than the experimental resolution, and we consider that this is the reason why we find no characteristic feature in the voltage measurements (Fig. 5A).

Downloaded from http://advances.sciencemag.org/ on January 24, 2021

Table 1. Parameters used to describe the experimental results. Resistivity (ρ_N), Seebeck coefficient (S_N), spin diffusion length (λ_N), spin Hall angle (θ_{SH}), and spin Nernst angle (θ_{SN}) of the HM layer and resistivity (ρ_F), Seebeck coefficient (S_F), anomalous Hall angle (θ_{AH}), and anomalous Nernst angle (θ_{AN}) of the FM layer in the HM/FM/MgO heterostructure. Re[G_{MIX}] and Im[G_{MIX}] represent the real and imaginary parts of the spin-mixing conductance G_{MIX} at the HM/FM interface. N/A, not applicable. Ω, ohm; μΩ, microohm.

Film structure	HM layer					FM layer				Interface	
	ρ_N (μΩ·cm)	S_N (μV/K)	λ_N (nm)	θ_{SH}	θ_{SN}	ρ_F (μΩ·cm)	S_F (μV/K)	θ_{AH}	θ_{AN}	Re[G_{MIX}] (Ω^{-1} cm^{-2})	Im[G_{MIX}] (Ω^{-1} cm^{-2})
Ta/CoFeB	183	−2	0.5	−0.13	N/A	160	−4	0.04	−0.25	2×10^{10}	-20×10^{10}
W/CoFeB	130	−12	1.1	−0.28	Varied	160	−4	0.04	−0.25	2×10^{10}	-5×10^{10}

Furthermore, we show that the spin Nernst angle θ_{SN} can be extracted experimentally, without relying on model parameters such as the spin mixing conductance. From Eqs. 1 and 5, we obtain

$$\frac{\theta_{SN}}{\theta_{SH}} = \frac{S}{S_N}\left[\frac{S_{SNE}}{SR_{SMR}} + 1\right] \quad (7)$$

In Fig. 5D, we plot θ_{SN}/θ_{SH} obtained by using the results of Figs. 1D, 3E, and 5C (and Eq. 7). The plot shows that the signs of the spin Nernst and spin Hall angles are opposite and the magnitude of the former is somewhat smaller than that of the latter. [Meyer *et al.* (*49*) have studied the spin Nernst effect in Pt/YIG and found that the signs of two angles are also opposite for Pt; however, the spin Nernst angle of Pt was reported to be larger than its spin Hall angle].

From numerical calculations, we find that θ_{SN}/θ_{SH} is not susceptible to the values of the spin-mixing conductance and the degree of longitudinal spin absorption (that is, the spin polarization of the FM layer), which influences the absolute values of R_{SMR} and S_{SNE} (*31*). The calculations also show that θ_{SN}/θ_{SH} is not significantly influenced by contribution(s) from the anomalous Hall/anomalous Nernst effects and the spin Hall/spin Nernst effects, if any, of the FM layer as long as the HM layer thickness d_N is larger than λ_N (details will be reported elsewhere). When d_N is smaller than λ_N, these effects can influence the value of θ_{SN}/θ_{SH}: The slight increase in θ_{SN}/θ_{SH} at small d_N found in Fig. 5D may be due to this contribution. We thus consider that the large d_N limit of θ_{SN}/θ_{SH} provides a better estimate, from which we find $\theta_{SN}/\theta_{SH} \sim -0.7$.

DISCUSSION

The anomalous Nernst and anomalous Hall angles (*50*–*54*) of CoFeB also have opposite signs (see Table 1), which results in a larger anomalous Nernst effect than otherwise. Theoretically, the signs of the Nernst and Hall angles do not necessarily have to match (*33*), since the Nernst angle (θ_{AN} and θ_{SN}) is defined by the energy derivative of the corresponding Hall conductivity near the Fermi energy, which can be positive or negative regardless of the sign of the Hall angle (θ_{AH} and θ_{SH}). Thus, the sign and the magnitude of the Nernst angle can be very different from the Hall angle. The recently reported spin Hall tunneling spectroscopy (*55*) and/or the temperature gradient–induced magnetization measurements (*56*) may provide access to information on the energy-level dependence of the Hall conductivity and can be used to verify the relationship between the Hall and Nernst angles.

We briefly discuss contributions from other effects that may influence the signal due to the spin Nernst effect (see table S1 for more details). It has been reported that an unintended out-of-plane temperature gradient may develop during the application of an in-plane temperature gradient (*15*, *43*–*45*). Under this circumstance, the anomalous Nernst effect of the FM layer can contaminate the signals observed in the voltage measurements. We observe this longitudinal voltage (V_{XX}) in film structures without the HM (W) layer and thicker FM (CoFeB) layer under the application of H_Y. However, the H_Y dependence of V_{XX} is distinct: The values of V_{XX} when the magnetization points along $+y$ and $-y$ are different for the anomalous Nernst voltage caused by the unintended out-of-plane temperature gradient (fig. S3, L to N), whereas the values lie at the same level for the spin Nernst coefficient induced by the in-plane temperature gradient (Fig. 5B). For similar reasons, the combined effect of the spin Seebeck effect within the FM layer and the inverse SHE of the HM layer under an out-of-plane temperature gradient can be excluded. The size of the unintended out-of-plane temperature gradient scales with the thickness of the CoFeB layer, and it is smaller than the detection limit for the 1-nm-thick CoFeB layer used here (see fig. S3, I to N). We have also confirmed that the spin Nernst coefficient S_{SNE} is negligible for heterostructures without the W layer (for example, in sub.|1 CoFeB|2 MgO|1 Ta) (see fig. S3, K to N).

The results presented here not only provide insights into the thermoelectric generation of spin current in HMs with strong spin-orbit coupling but also have important implications on expanding the search of materials that can generate spin current. The spin Nernst effect may be able to generate spin current from materials that are not possible with the SHE, for example, in systems where the density of states at the Fermi level is zero. The two-dimensional chalcogenides and the Weyl semimetals, in which the Fermi level coincides with the Dirac point, are of particular interest. The spin Nernst effect may thus broaden material research on the spin current generation beyond the current reach of the SHE.

MATERIALS AND METHODS

Sample preparation and measurements

All films were deposited using magnetron sputtering on nondoped silicon substrates coated with ~100-nm-thick thermal oxides (SiO_x). Films were post-annealed at ~300°C for 1 hour before the device patterning processes. Optical lithography and Ar ion etching were used to pattern the films into wires and Hall bars. Contact pads made of 5 Ta|100 Au (in nanometers) were formed by a liftoff process.

All measurements were performed at room temperature. A temperature gradient across the substrate was applied by placing a ceramic

Downloaded from http://advances.sciencemag.org/ on January 24, 2021

heater on one side of the substrate and a heat-absorbing Cu block on the other side. The substrate was fixed to the heater/Cu block using a thermally conducting double-sided tape made of Al. The temperature profile of the system was studied using an infrared camera with Si substrates coated with a blackbody matt (the surface emissivity is calibrated). The camera was used to ensure that the temperature gradient across the substrate is uniform. Because of the necessity of this coating, the temperature profile of the device under investigation cannot be monitored in real time: Once the sample is coated with the blackbody matt, it is difficult to perform the voltage measurements. Since the temperature gradient across the substrate largely depends on the contact between the substrate and the heater/Cu block, we checked its variation by placing the substrate to the setup multiple times and monitored the temperature profile using the infrared camera. The variation of the temperature gradient was ~±10% of the average value. The horizontal error bars in Figs. 3 (B and C) and 4C reflect this variation. The vertical error bars in the same figures represent the distribution of the voltage when measurements are repeated multiple times under the same contact between the substrate and the heater/Cu block. The vertical error bars are smaller than the symbols, suggesting that the measurements are stable and the temperature gradient do not evolve once the substrate is fixed. Thus, the dominant source of the measurement error originates from the uncertainty in the actual value of the temperature gradient across the substrate: The error bars in Figs. 3 (D and E), 4 (D to G), and 5 (C and D) reflect this uncertainty.

Fitting procedure

Experimental results were fitted using Eqs. 1, 2, 5, and 6. Before carrying out the fitting, we determined the following parameters from the experimental results. The resistivity (ρ_N) of the HM layers was obtained by the d_N dependence of G_{XX} shown in Fig. 1 (A and B). For the resistivity (ρ_F) of the FM (CoFeB) layer, we used a value from our previous study (*57*). The Seebeck coefficients of the HM layer (S_N) and the FM layer (S_F) were estimated from the results presented in Fig. 3 (D and E). We also measured the Seebeck coefficient of the FM layer (S_F) independently using a film stack that did not include any HM layer (results are shown in fig. S4I). We found that S_F estimated from film stacks with and without the HM layer were similar. The anomalous Hall angle (θ_{AH}) and the anomalous Nernst angle (θ_{AN}) of the FM (CoFeB) layer can be estimated by the zero HM thickness limit of the normalized R_{AHE} (Fig. 2, C and D) and the normalized S_{ANE} (Fig. 4, F and G), respectively.

We first fit R_{SMR} (Fig. 1, C and D) and R_{AHE} (Fig. 2, C and D) using Eqs. 1 and 2 to determine θ_{SH}, λ_N, Re[G_{MIX}], and Im[G_{MIX}]. Note that in many previous studies, a transparent interface [Re[G_{MIX}] ≫ Im[G_{MIX}] and Re[G_{MIX}] ≫ $1/(2\rho_N\lambda_N)$] has been assumed to estimate the lower bound of θ_{SH}. In such a case, G_{MIX} drops off from Eq. 1 and simplifies the fitting. Here, we used Re[G_{MIX}] and Im[G_{MIX}] as the fitting parameters to account for the d_N dependence of R_{SMR} and R_{AHE}. For both underlayer films, we found that Im[G_{MIX}] has to be negative and larger in magnitude than Re[G_{MIX}]. This characteristic G_{MIX} is in agreement with the current induced torque found in similar heterostructures (*58*–*60*) according to the relation of G_{MIX} and the torque (*61*). For the Ta underlayer films, the change in R_{AHE} with d_N is larger than what is expected from Eq. 2. We infer that there are other effects that are not captured by Eq. 2 (*62*, *63*). With the parameters described in Table 1 (unless noted otherwise), S_{SNE} (Fig. 5C) and S_{ANE} (Fig. 4, F and G) were calculated using Eqs. 5 and 6, respectively, with θ_{SN} denoted in each figure legend.

SUPPLEMENTARY MATERIALS

Supplementary material for this article is available at http://advances.sciencemag.org/cgi/content/full/3/11/e1701503/DC1

Additional experimental results

Discussion related to other effects that may influence the voltage measurements

fig. S1. Magnetic properties of HM/CoFeB/MgO heterostructures.

fig. S2. Spin Nernst magnetoresistance of Ta and W underlayer films.

fig. S3. Thermoelectric properties of CoFeB thin films without the HM layer.

fig. S4. Comparison of parameters with and without the HM layer.

table S1. Influence of other phenomena on the temperature gradient–induced voltage measurements.

REFERENCES AND NOTES

1. M. I. Dyakonov, V. I. Perel, Current-induced spin orientation of electrons in semiconductors. *Phys. Lett. A* **35**, 459–460 (1971).
2. L. Liu, C.-F. Pai, Y. Li, H. W. Tseng, D. C. Ralph, R. A. Buhrman, Spin-torque switching with the giant spin Hall effect of tantalum. *Science* **336**, 555–558 (2012).
3. A. Hoffmann, Spin Hall effects in metals. *IEEE Trans. Magn.* **49**, 5172–5193 (2013).
4. T. Jungwirth, J. Wunderlich, K. Olejnik, Spin Hall effect devices. *Nat. Mater.* **11**, 382–390 (2012).
5. M. Morota, Y. Niimi, K. Ohnishi, D. H. Wei, T. Tanaka, H. Kontani, T. Kimura, Y. Otani, Indication of intrinsic spin Hall effect in 4*d* and 5*d* transition metals. *Phys. Rev. B* **83**, 174405 (2011).
6. J. Liu, T. Ohkubo, S. Mitani, K. Hono, M. Hayashi, Correlation between the spin Hall angle and the structural phases of early 5*d* transition metals. *Appl. Phys. Lett.* **107**, 232408 (2015).
7. G. Y. Guo, S. Murakami, T.-W. Chen, N. Nagaosa, Intrinsic spin Hall effect in platinum: First-principles calculations. *Phys. Rev. Lett.* **100**, 096401 (2008).
8. T. Tanaka, H. Kontani, M. Naito, T. Naito, D. S. Hirashima, K. Yamada, J. Inoue, Intrinsic spin Hall effect and orbital Hall effect in 4*d* and 5*d* transition metals. *Phys. Rev. B* **77**, 165117 (2008).
9. K. Uchida, S. Takahashi, K. Harii, J. Ieda, W. Koshibae, K. Ando, S. Maekawa, E. Saitoh, Observation of the spin Seebeck effect. *Nature* **455**, 778–781 (2008).
10. G. E. W. Bauer, E. Saitoh, B. J. van Wees, Spin caloritronics. *Nat. Mater.* **11**, 391–399 (2012).
11. J. Xiao, G. E. W. Bauer, K.-c. Uchida, E. Saitoh, S. Maekawa, Theory of magnon-driven spin Seebeck effect. *Phys. Rev. B* **81**, 214418 (2010).
12. K. Uchida, J. Xiao, H. Adachi, J. Ohe, S. Takahashi, J. Ieda, T. Ota, Y. Kajiwara, H. Umezawa, H. Kawai, G. E. W. Bauer, S. Maekawa, E. Saitoh, Spin Seebeck insulator. *Nat. Mater.* **9**, 894–897 (2010).
13. C. M. Jaworski, J. Yang, S. Mack, D. D. Awschalom, J. P. Heremans, R. C. Myers, Observation of the spin-Seebeck effect in a ferromagnetic semiconductor. *Nat. Mater.* **9**, 898–903 (2010).
14. A. Slachter, F. L. Bakker, J.-P. Adam, B. J. van Wees, Thermally driven spin injection from a ferromagnet into a non-magnetic metal. *Nat. Phys.* **6**, 879–882 (2010).
15. S. Y. Huang, W. G. Wang, S. F. Lee, J. Kwo, C. L. Chien, Intrinsic spin-dependent thermal transport. *Phys. Rev. Lett.* **107**, 216604 (2011).
16. G.-M. Choi, C.-H. Moon, B.-C. Min, K.-J. Lee, D. G. Cahill, Thermal spin-transfer torque driven by the spin-dependent Seebeck effect in metallic spin-valves. *Nat. Phys.* **11**, 576–581 (2015).
17. L. J. Cornelissen, J. Liu, R. A. Duine, J. Ben Youssef, B. J. van Wees, Long-distance transport of magnon spin information in a magnetic insulator at room temperature. *Nat. Phys.* **11**, 1022–1026 (2015).
18. S.-g. Cheng, Y. Xing, Q.-f. Sun, X. C. Xie, Spin Nernst effect and Nernst effect in two-dimensional electron systems. *Phys. Rev. B* **78**, 045302 (2008).
19. Z. Ma, Spin Hall effect generated by a temperature gradient and heat current in a two-dimensional electron gas. *Solid State Commun.* **150**, 510–513 (2010).
20. K. Tauber, M. Gradhand, D. V. Fedorov, I. Mertig, Extrinsic spin Nernst effect from first principles. *Phys. Rev. Lett.* **109**, 026601 (2012).
21. S. Wimmer, D. Ködderitzsch, K. Chadova, H. Ebert, First-principles linear response description of the spin Nernst effect. *Phys. Rev. B* **88**, 201108(R) (2013).
22. G. Géranton, F. Freimuth, S. Blügel, Y. Mokrousov, Spin-orbit torques in $L1_0$–FePt/Pt thin films driven by electrical and thermal currents. *Phys. Rev. B* **91**, 014417 (2015).
23. K. Tauber, D. V. Fedorov, M. Gradhand, I. Mertig, Spin Hall and spin Nernst effect in dilute ternary alloys. *Phys. Rev. B* **87**, 161114(R) (2013).
24. C.-F. Pai, L. Liu, Y. Li, H. W. Tseng, D. C. Ralph, R. A. Buhrman, Spin transfer torque devices utilizing the giant spin Hall effect of tungsten. *Appl. Phys. Lett.* **101**, 122404 (2012).
25. Q. Hao, W. Chen, G. Xiao, Beta (β) tungsten thin films: Structure, electron transport, and giant spin Hall effect. *Appl. Phys. Lett.* **106**, 182403 (2015).
26. Y.-T. Chen, S. Takahashi, H. Nakayama, M. Althammer, S. T. B. Goennenwein, E. Saitoh, G. E. W. Bauer, Theory of spin Hall magnetoresistance. *Phys. Rev. B* **87**, 144411 (2013).

Downloaded from http://advances.sciencemag.org/ on January 24, 2021

27. H. Nakayama, M. Althammer, Y.-T. Chen, K. Uchida, Y. Kajiwara, D. Kikuchi, T. Ohtani, S. Geprägs, M. Opel, S. Takahashi, R. Gross, G. E. W. Bauer, S. T. B. Goennenwein, E. Saitoh, Spin Hall magnetoresistance induced by a nonequilibrium proximity effect. *Phys. Rev. Lett.* **110**, 206601 (2013).
28. M. Althammer, S. Meyer, H. Nakayama, M. Schreier, S. Altmannshofer, M. Weiler, H. Huebl, S. Geprägs, M. Opel, R. Gross, D. Meier, C. Klewe, T. Kuschel, J.-M. Schmalhorst, G. Reiss, L. Shen, A. Gupta, Y.-T. Chen, G. E. W. Bauer, E. Saitoh, S. T. B. Goennenwein, Quantitative study of the spin Hall magnetoresistance in ferromagnetic insulator/normal metal hybrids. *Phys. Rev. B* **87**, 224401 (2013).
29. C. Hahn, G. de Loubens, O. Klein, M. Viret, V. V. Naletov, J. Ben Youssef, Comparative measurements of inverse spin Hall effects and magnetoresistance in YIG/Pt and YIG/Ta. *Phys. Rev. B* **87**, 174417 (2013).
30. C. O. Avci, K. Garello, A. Ghosh, M. Gabureac, S. F. Alvarado, P. Gambardella, Unidirectional spin Hall magnetoresistance in ferromagnet/normal metal bilayers. *Nat. Phys.* **11**, 570–575 (2015).
31. J. Kim, P. Sheng, S. Takahashi, S. Mitani, M. Hayashi, Spin Hall magnetoresistance in metallic bilayers. *Phys. Rev. Lett.* **116**, 097201 (2016).
32. S. M. Rossnagel, I. C. Noyan, C. Cabral Jr., Phase transformation of thin sputter-deposited tungsten films at room temperature. *J. Vac. Sci. Technol. B* **20**, 2047 (2002).
33. N. F. Mott, H. Jones, *The Theory of the Properties of Metals and Alloys* (Dover Publications, 1958).
34. S. Meyer, R. Schlitz, S. Geprägs, M. Opel, H. Huebl, R. Gross, S. T. B. Goennenwein, Anomalous Hall effect in YIG|Pt bilayers. *Appl. Phys. Lett.* **106**, 132402 (2015).
35. P. Krzysteczko, X. Hu, N. Liebing, S. Sievers, H. W. Schumacher, Domain wall magneto-Seebeck effect. *Phys. Rev. B* **92**, 140405(R) (2015).
36. T. R. McGuire, R. I. Potter, Anisotropic magnetoresistance in ferromagnetic 3*d* alloys. *IEEE Trans. Magn.* **11**, 1018–1038 (1975).
37. A. Kobs, S. Heße, W. Kreuzpaintner, G. Winkler, D. Lott, P. Weinberger, A. Schreyer, H. P. Oepen, Anisotropic interface magnetoresistance in Pt/Co/Pt sandwiches. *Phys. Rev. Lett.* **106**, 217207 (2011).
38. S. S.-L. Zhang, S. Zhang, Angular dependence of anisotropic magnetoresistance in magnetic systems. *J. Appl. Phys.* **115**, 17C703 (2014).
39. Y. M. Lu, J.-W. Cai, S.-Y. Huang, D. Qu, B. F. Miao, C.-L. Chien, Hybrid magnetoresistance in the proximity of a ferromagnet. *Phys. Rev. B* **87**, 220409(R) (2013).
40. J. Li, M. W. Jia, Z. Ding, J. Liang, Y. Luo, Y. Wu, Pt-enhanced anisotropic magnetoresistance in Pt/Fe bilayers. *Phys. Rev. B* **90**, 214415 (2014).
41. T. Kikkawa, K. Uchida, S. Daimon, Y. Shiomi, H. Adachi, Z. Qiu, D. Hou, X.-F. Jin, S. Maekawa, E. Saitoh, Separation of longitudinal spin Seebeck effect from anomalous Nernst effect: Determination of origin of transverse thermoelectric voltage in metal/insulator junctions. *Phys. Rev. B* **88**, 214403 (2013).
42. V. L. Grigoryan, W. Guo, G. E. W. Bauer, J. Xiao, Intrinsic magnetoresistance in metal films on ferromagnetic insulators. *Phys. Rev. B* **90**, 161412 (2014).
43. S. Bosu, Y. Sakuraba, K. Uchida, K. Saito, T. Ota, E. Saitoh, K. Takanashi, Spin Seebeck effect in thin films of the Heusler compound Co_2MnSi. *Phys. Rev. B* **83**, 224401 (2011).
44. D. Meier, D. Reinhardt, M. Schmid, C. H. Back, J.-M. Schmalhorst, T. Kuschel, G. Reiss, Influence of heat flow directions on Nernst effects in Py/Pt bilayers. *Phys. Rev. B* **88**, 184425 (2013).
45. M. Schmid, S. Srichandan, D. Meier, T. Kuschel, J.-M. Schmalhorst, M. Vogel, G. Reiss, C. Strunk, C. H. Back, Transverse spin Seebeck effect versus anomalous and planar Nernst effects in permalloy thin films. *Phys. Rev. Lett.* **111**, 187201 (2013).
46. B. F. Miao, S.-Y. Huang, D. Qu, C.-L. Chien, Inverse spin Hall effect in a ferromagnetic metal. *Phys. Rev. Lett.* **111**, 066602 (2013).
47. A. Tsukahara, Y. Ando, Y. Kitamura, H. Emoto, E. Shikoh, M. P. Delmo, T. Shinjo, M. Shiraishi, Self-induced inverse spin Hall effect in permalloy at room temperature. *Phys. Rev. B* **89**, 235317 (2014).
48. J. Cramer, F. Fuhrmann, U. Ritzmann, V. Gall, T. Niizeki, R. Ramos, Z. Qiu, D. Hou, T. Kikkawa, J. Sinova, U. Nowak, E. Saitoh, M. Kläui, Ferroic collinear multilayer magnon spin valve. http://arxiv.org/abs/1706.07592 (2017).
49. S. Meyer, Y.-T. Chen, S. Wimmer, M. Althammer, T. Wimmer, R. Schlitz, S. Geprägs, H. Huebl, D. Ködderitzsch, H. Ebert, G. E. W. Bauer, R. Gross, S. T. B. Goennenwein, Observation of the spin Nernst effect. *Nat. Mater.* **16**, 977–981 (2017).
50. T. Miyasato, N. Abe, T. Fujii, A. Asamitsu, S. Onoda, Y. Onose, N. Nagaosa, Y. Tokura, Crossover behavior of the anomalous Hall effect and anomalous Nernst effect in itinerant ferromagnets. *Phys. Rev. Lett.* **99**, 086602 (2007).
51. Y. Pu, D. Chiba, F. Matsukura, H. Ohno, J. Shi, Mott relation for anomalous Hall and Nernst effects in $Ga_{1-x}Mn_xAs$ ferromagnetic semiconductors. *Phys. Rev. Lett.* **101**, 117208 (2008).
52. K. Hasegawa, M. Mizuguchi, Y. Sakuraba, T. Kamada, T. Kojima, T. Kubota, S. Mizukami, T. Miyazaki, K. Takanashi, Material dependence of anomalous Nernst effect in perpendicularly magnetized ordered-alloy thin films. *Appl. Phys. Lett.* **106**, 252405 (2015).
53. C. Fang, C. H. Wan, Z. H. Yuan, L. Huang, X. Zhang, H. Wu, Q. T. Zhang, X. F. Han, Scaling relation between anomalous Nernst and Hall effect in $[Pt/Co]_n$ multilayers. *Phys. Rev. B* **93**, 054420 (2016).
54. T. Zhu, P. Chen, Q. H. Zhang, R. C. Yu, B. G. Liu, Giant linear anomalous Hall effect in the perpendicular CoFeB thin films. *Appl. Phys. Lett.* **104**, 202404 (2014).
55. L. Liu, C.-T. Chen, J. Z. Sun, Spin Hall effect tunnelling spectroscopy. *Nat. Phys.* **10**, 561–566 (2014).
56. D. Hou, Z. Qiu, R. Iguchi, K. Sato, E. K. Vehstedt, K. Uchida, G. E. W. Bauer, E. Saitoh, Observation of temperature-gradient-induced magnetization. *Nat. Commun.* **7**, 12265 (2016).
57. J. Torrejon, J. Kim, J. Sinha, S. Mitani, M. Hayashi, M. Yamanouchi, H. Ohno, Interface control of the magnetic chirality in CoFeB/MgO heterostructures with heavy-metal underlayers. *Nat. Commun.* **5**, 4655 (2014).
58. J. Kim, J. Sinha, M. Hayashi, M. Yamanouchi, S. Fukami, T. Suzuki, S. Mitani, H. Ohno, Layer thickness dependence of the current-induced effective field vector in Ta|CoFeB|MgO. *Nat. Mater.* **12**, 240–245 (2013).
59. K. Garello, I. M. Miron, C. O. Avci, F. Freimuth, Y. Mokrousov, S. Blügel, S. Auffret, O. Boulle, G. Gaudin, P. Gambardella, Symmetry and magnitude of spin–orbit torques in ferromagnetic heterostructures. *Nat. Nanotechnol.* **8**, 587–593 (2013).
60. C.-F. Pai, Y. Ou, L. H. Vilela-Leão, D. C. Ralph, R. A. Buhrman, Dependence of the efficiency of spin Hall torque on the transparency of Pt/ferromagnetic layer interfaces. *Phys. Rev. B* **92**, 064426 (2015).
61. A. Brataas, G. E. W. Bauer, P. J. Kelly, Non-collinear magnetoelectronics. *Phys. Rep.* **427**, 157–255 (2006).
62. Z. B. Guo, W. B. Mi, R. O. Aboljadayel, B. Zhang, Q. Zhang, P. G. Barba, A. Manchon, X. Zhang, Effects of surface and interface scattering on anomalous Hall effect in Co/Pd multilayers. *Phys. Rev. B* **86**, 104433 (2012).
63. V. Keskin, B. Aktaş, J. Schmalhorst, G. Reiss, H. Zhang, J. Weischenberg, Y. Mokrousov, Temperature and Co thickness dependent sign change of the anomalous Hall effect in Co/Pd multilayers: An experimental and theoretical study. *Appl. Phys. Lett.* **102**, 022416 (2013).

Acknowledgments: We thank S. Bosu and S.S.-L. Zhang for fruitful discussions. **Funding:** This work was partly supported by Japan Society for the Promotion of Science (JSPS) Grants-in-Aid (15H05702 and 26709045), Casio Foundation, Ministry of Education, Culture, Sports, Science and Technology (MEXT) R&D Next-Generation Information Technology, and the Spintronics Research Network of Japan. Y.-C.L. is an International Research Fellow of the JSPS. **Author contributions:** M.H. and Y.S. planned the study. P.S. and Y.-C.L. carried out microfabrication. P.S., Y.-C.L., and Y.S. measured the samples and analyzed the results with help from S.M. and M.H. S.T. developed the drift-diffusion model. All authors discussed the data and commented on the manuscript. **Competing interests:** The authors declare that they have no competing interests. **Data and materials availability:** All data needed to evaluate the conclusions in the paper are present in the paper and/or the Supplementary Materials. Additional data related to this paper may be requested from the authors.

Submitted 8 May 2017
Accepted 4 October 2017
Published 3 November 2017
10.1126/sciadv.1701503

Citation: P. Sheng, Y. Sakuraba, Y.-C. Lau, S. Takahashi, S. Mitani, M. Hayashi, The spin Nernst effect in tungsten. *Sci. Adv.* **3**, e1701503 (2017).

Downloaded from http://advances.sciencemag.org/ on January 24, 2021

Science Advances

The spin Nernst effect in tungsten

Peng Sheng, Yuya Sakuraba, Yong-Chang Lau, Saburo Takahashi, Seiji Mitani and Masamitsu Hayashi

Sci Adv **3** (11), e1701503.
DOI: 10.1126/sciadv.1701503

ARTICLE TOOLS http://advances.sciencemag.org/content/3/11/e1701503

SUPPLEMENTARY MATERIALS http://advances.sciencemag.org/content/suppl/2017/10/30/3.11.e1701503.DC1

REFERENCES This article cites 60 articles, 1 of which you can access for free
http://advances.sciencemag.org/content/3/11/e1701503#BIBL

PERMISSIONS http://www.sciencemag.org/help/reprints-and-permissions

Use of this article is subject to the Terms of Service

Science Advances (ISSN 2375-2548) is published by the American Association for the Advancement of Science, 1200 New York Avenue NW, Washington, DC 20005. The title *Science Advances* is a registered trademark of AAAS.

Copyright © 2017 The Authors, some rights reserved; exclusive licensee American Association for the Advancement of Science. No claim to original U.S. Government Works. Distributed under a Creative Commons Attribution NonCommercial License 4.0 (CC BY-NC).

Downloaded from http://advances.sciencemag.org/ on January 24, 2021